The value of S_p for isotropic particle bombardment as given in Table 4 varies from about 5,000 erg cm^{-2} sec^{-1} for Callisto to about 14,000 erg cm^{-2} sec^{-1} for Io and Europa for equilibrium with the hemispheres of the satellites. For equilibrium over the entire sphere the energy flux required ranges from about 20,000 to about 40,000 erg cm^{-2} sec^{-1}, depending on the satellite. All of these fluxes are needed if the particles impinge on the satellites from all directions. Still greater fluxes are required for unidirectional particles.

The flux range 5,000 to 14,000 erg cm^{-2} sec^{-1} is about one order of magnitude greater than particle energy fluxes measured on the Pioneer 10 and Pioneer 11 missions (*4*). The larger required particle energy flux may be reasonable, however, since in the particle measurements the usually numerous kilovolt and lower-energy particles have not been included. On the other hand, particle energy fluxes required for equilibrium on a total spherical basis are of the order of two magnitudes greater than the measured flux rates. Such large fluxes may be questionable, unless by some peculiar coincidence Pioneer 10 and Pioneer 11 visited the vicinity of Jupiter during quiescent periods. Present information precludes any judgment on such a possibility. There may also be errors in the measurements that may mitigate the flux requirements. Some focusing of particles near the satellite may also be possible if there is some net charging of the satellites. These satellites may also be surrounded by plasma as for artificial earth satellites in the ionosphere.

In view of Io's apparently violent reactions to such particle bombardment with the release of sodium to the surrounding space, one should also look for similar clouds about the other Galilean satellites. Their much larger gravitational spheres of influence, however, may lessen the likelihood of such discoveries. Amalthea, closer to Jupiter and smaller than the Galilean satellites, may exhibit even more violent effects of bombardment than for the Galilean satellites.

STANLEY H. GROSS
Department of Electrical Engineering and Electrophysics, Polytechnic Institute of New York, Farmingdale 11735

References and Notes

1. D. Morrison and D. P. Cruikshank, *Space Sci. Rev.* **15**, 641 (1974).
2. Albedo is a synonym for reflectivity, but it is usually modified by qualifying words. The Bond albedo is the ratio of the total light power reflected in all directions from a body to the total light power incident on it in a collimated beam. It is the fraction of the incident solar flux that is not absorbed. The Bond albedo is the product of the geometric albedo and the phase integral. The geometric albedo is the ratio of the power per unit solid angle per unit projected area at full phase (phase angle is zero) to the power per unit solid angle per unit projected area of a perfectly diffusing disk in the same position and with the same apparent size as the planet or satellite. The disk is taken to be normal to the source of illumination (the sun). The perfectly diffusing disk absorbs no power and scatters all incident flux according to Lambert's law. The phase angle is the planet- or satellite-centered angle between the source of illumination (the sun) and the observer (or detector). The phase integral is the ratio of power scattered in all directions to that scattered at zero phase per unit solid angle. For a nonspecialist, additional information on this terminology may be found in: S. K. Runcorn *et al.*, Eds., *International Dictionary of Geophysics* (Pergamon, Oxford, 1967), vol. 1; R. W. Fairbridge, Ed., *Encyclopedia of Atmospheric Sciences and Astrogeology* (Reinhold, New York, 1967).
3. J. A. Simpson, D. C. Hamilton, G. A. Lentz, R. B. McKibben, M. Perkins, K. R. Pyle, A. J. Tuzzolino, J. J. O'Gallagher, *Science* **188**, 455 (1975); J. H. Trainor, F. B. McDonald, D. E. Stilwell, B. J. Teegarden, W. R. Webber, *ibid.*, p. 462; J. A. Van Allen, B. A. Randall, D. N. Baker, C. K. Goertz, D. D. Sentman, M. F. Thomsen, H. R. Flindt, *ibid.*, p. 459.
4. R. W. Fillius, C. E. McIlwain, A. Mogro-Campero, *ibid.*, p. 465.
5. This work was supported in part by NASA grant NGR-33-006-068.

27 May 1975; revised 2 July 1975

Magnetotelluric Sounding of Permafrost

Abstract. *The audio-frequency magnetotelluric method was used to sound a permafrost region in the Mackenzie delta in the Northwest Territories. A simple two-layer model consisting of a high electrical resistivity layer overlying less resistive material gave interpreted depths in agreement with those determined by drilling. The summer active layer was transparent even at high sounding frequencies.*

The mapping of permafrost thickness in the Arctic is an important problem having applications ranging from the construction of pipelines to the interpretation of seismic data. Electrically, the transition from frozen to unfrozen earth is generally accompanied by a significant decrease in resistivity (*1*). The problem of measuring permafrost thickness then becomes one of measuring the depth to this electrical interface.

Audio-frequency magnetotellurics (AMT), an extension of the basic magnetotelluric method first proposed by Cagniard (*2*), is a system which utilizes naturally occurring telluric currents that are induced by distant lightning discharges. These "sferics" propagate in the earth-ionosphere cavity and with sensitive instrumentation can be detected many thousands of miles away. By use of grounded electric dipoles 100 feet ($\sim$ 30 m) in length and a broadband induction coil, coherent sferic pulses in the electric and magnetic fields are passed through narrow band pass filters and the ratio of the average electric field strength to the average magnetic field strength is electronically determined (*3*).

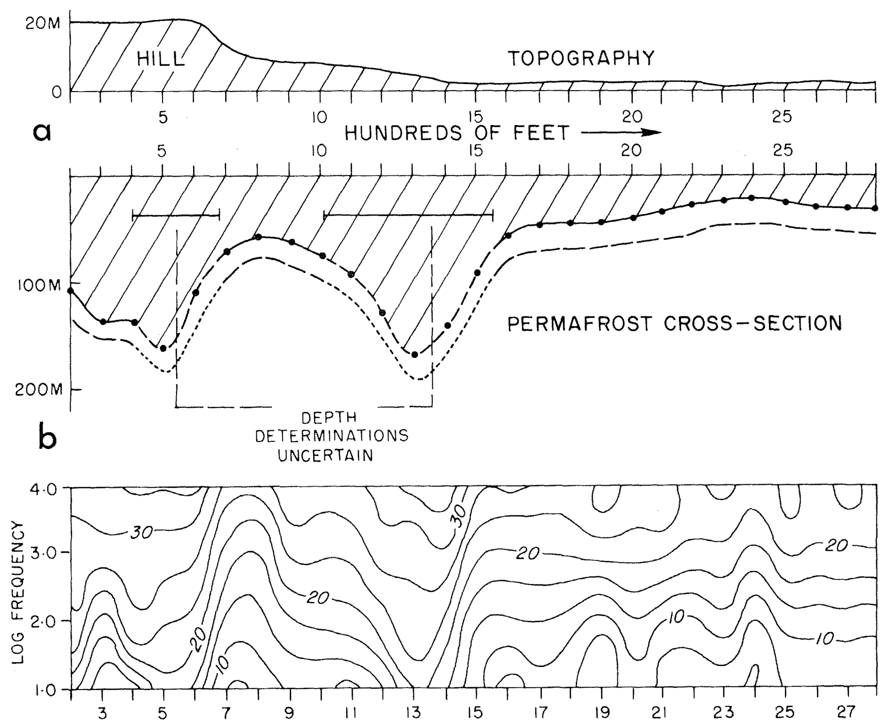

Fig. 1. (a) Topographic cross section of survey profile. The hill is a vestige of an areal ice sheet. (b) Permafrost cross section determined at 10 khz using a two-layer model. (c) Pseudosection representation of data indicating both lateral and vertical variations in resistivity. Labeled contours are intervals of 10 log ρ_a. The electric field was measured across the profile.

This ratio is then used to compute a frequency-dependent scalar apparent resistivity ρ_a (*2*).

An AMT survey was conducted in the Arctic over a zone of permafrost and ice at the Involuted Hill (*4*) near Tuktoyuktuk, Northwest Territories, at the mouth of the Mackenzie River. Apparent resistivities were measured in two orthogonal directions every 100 feet along profiles. A topographic cross section of one of these profiles is shown in Fig. 1a. The hill stands about 20 m above the plain and is believed to be the residual part of a large areal ice sheet that grew in place after retreat of the glacial ice and was subsequently covered with clay and till deposits. In the surrounding valley there is a more or less uniform sheet of permafrost, which thickens toward the hill and then plunges to form a much deeper permafrost root.

In our experiment, apparent resistivities were measured at 11 frequencies spaced approximately logarithmically from 10 hertz to 10 khz. The data at each station (log frequency versus log resistivity) were fitted by a least-squares cubic polynomial, which was then equidistantly interpolated for machine contouring (*5*) into pseudosections—a format that conveniently displays both lateral variations in resistivity and variations in resistivity with frequency. In a pseudosection (Fig. 1c) a horizontal gradient in contour lines indicates lateral variations in ρ_a, while a vertical gradient indicates a change in ρ_a with frequency. The pseudosection in Fig. 1c, which corresponds to the profile in Fig. 1a, is contoured in logarithmic intervals, each labeled contour line equaling ten times the logarithm of resistivity. In all cases, ρ_a decreases with decreasing frequency, indicating that the earth's true average resistivity must steadily decrease when averaged to increasing depths.

The simplest model that will produce this effect is a resistive layer over a relatively conducting half-space. Such a two-layer model and a schematic sounding curve are depicted in Fig. 2, a and b.

In the survey, particularly in the valley, the data collected generally lay along a 45° line, indicating that the resistivity of the upper layer was not being detected. In fact, this portion of the two-layer sounding curve, shown in Fig. 2b, is very insensitive to ρ_1, provided that the contrast in resistivity remains large. At the lowest frequencies ρ_a becomes totally independent of ρ_1. In the case of a highly resistive upper layer it becomes possible to derive a simple function that describes the frequency behavior of ρ_a (*6*).

$$\rho_a = \rho_2 \left(1 + \frac{2h}{\delta_2} + \frac{2h^2}{\delta_2^2}\right) \qquad (1)$$

where h is the permafrost thickness and ρ_2 is the skin depth in the lower medium (*7*). At high frequencies the third term dominates, making ρ_a independent of all electrical parameters. It then follows that

$$h = 356 \left(\frac{\rho_a}{f}\right)^{1/2} \qquad (2)$$

where f is frequency. These functions are sketched in Fig. 2c. Thus when the resistivity contrast between the permafrost and the underlying material is large it is possible to determine permafrost thickness by using just one frequency.

If the permafrost thickness becomes appreciable in terms of skin depths, if displacement currents become significant, or if a thick active layer is present (*8*), this analysis and model are still applicable, but over a more limited range of frequencies. The effect of each of these factors is to cause the curve to "roll over," starting with the highest frequencies—an effect which is easily identifiable in multifrequency data (Fig. 2c).

A three-station running average (*9*) was applied to the smooth data in the pseudosection of Fig. 1c, and the 10-khz observations were then used to determine the thickness of the upper layer, using Eq. 1 and an average resistivity of 50 ohm-m for the lower medium. The cross section derived in this way, using Eq. 1, is shown in Fig. 1b. The dotted line in Fig. 1b indicates the permafrost thickness obtained using Eq. 2.

In the valley, where the permafrost is roughly horizontal, there is good agreement between the computed permafrost thickness and the thickness obtained by drilling. On the hill, where there is considerable lateral variation, the use of a stratified model underestimates depth. However, AMT sharply delineates those regions of high lateral resistivity contrast where such a simple model is inappropriate. Regions where determined depths are questionable have been indicated by broken lines in Fig. 1b.

The magnetotelluric sounding results at the Involuted Hill show that permafrost may be successfully modeled as a two-layer case consisting of high-resistivity permafrost overlying a less resistive unfrozen layer. At lower audio frequencies the apparent resistivities obtained are insensitive

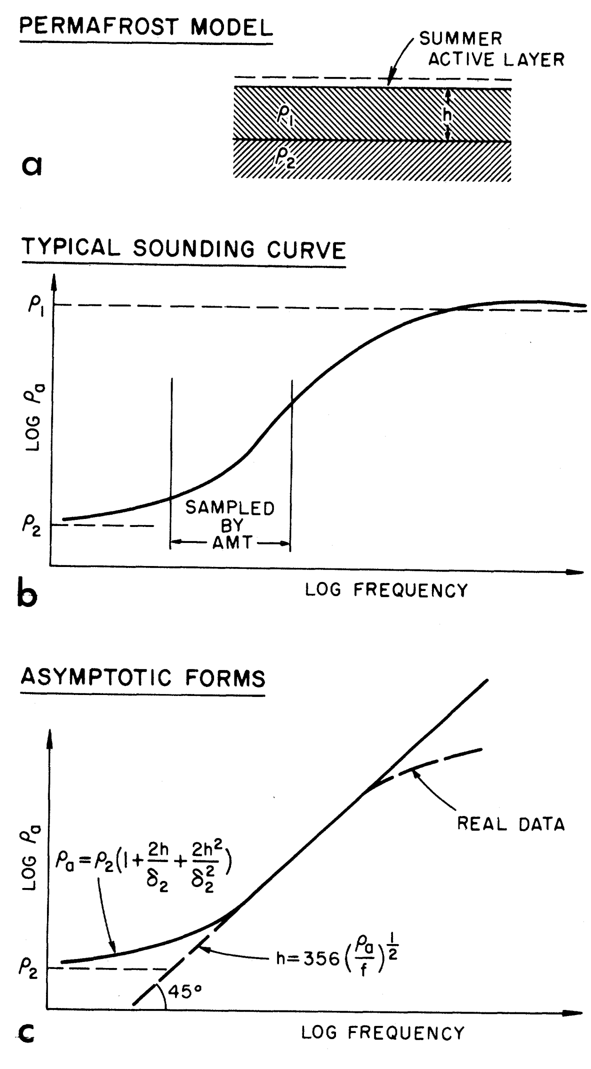

Fig. 2. (a) Permafrost model for $\rho_1 >> \rho_2$. A third active layer (dashed line) is present during summer. (b) Schematic frequency sounding curve indicating portion sampled by AMT. (c) Low-frequency asymptotic forms of two-layer response. Real data eventually roll over because of (i) the presence of a surface active layer, (ii) dielectric effects in permafrost, or (iii) a large conductivity-thickness product for the permafrost layer.

to the electrical properties of the upper frozen layer. The conducting active layer, which is always present in the summer and hampers such galvanic methods as d-c resistivity measurements (*10*), had essentially no effect on the data obtained.

ANDREW KOZIAR
Department of Physics, University of Toronto, Toronto, Ontario, Canada M5S 1A7
D. W. STRANGWAY
Department of Geology, University of Toronto

References and Notes

1. P. Hoekstra and D. McNeill, in *North American Contribution to the Second International Conference on Permafrost* (National Research Council–National Academy of Sciences, Washington, D.C., 1973), pp. 517–526.
2. L. Cagniard, *Geophysics* **18**, 605 (1953). The scalar apparent resistivity is defined as

$$\rho_a = \frac{1}{\omega\mu_0}\left|\frac{E_x}{H_y}\right|^2$$

where ω is angular frequency, μ_0 is the permeability of free space, E_x is electric field strength, and H_y is orthogonal magnetic field strength.
3. D. W. Strangway, C. Swift, R. Holmer, *ibid.* **38**, 1159 (1973).
4. The Involuted Hill test site has been extensively studied and drilled by the Geological Survey of Canada.
5. The contouring program was obtained from Y. Lamontagne.
6. At the permafrost–half-space interface one would determine that $E_0 = (i\omega\mu_0\rho_2)^{1/2}H_0$, E_0 and H_0 being orthogonal. In the permafrost itself $\nabla \times \mathbf{H} \simeq 0$ and $\nabla \times \mathbf{E} = i\omega\mu_0\mathbf{H}$. At the surface of the permafrost it follows that $H_y = H_0$ and $E_x = [(i\omega\mu_0\rho_2)^{1/2} + i\omega\mu_0 h]H_y$, where h is permafrost thickness. Defining ρ_a as in (*2*) and δ_2 as in (*7*), it follows that

$$\rho_a = \rho_2\left(1 + \frac{2h}{\delta 2} + \frac{2h^2}{\delta_2{}^2}\right)$$

7. Skin depth, $\delta_2 = (2\ \rho_2/\omega\mu_0)^{1/2}$, is the depth at which a plane wave has been attenuated to e^{-1} of its initial amplitude.
8. The apparent resistivity curve begins to roll over when $h \gtrsim 0.2\ \delta_2$, where δ_2 is the skin depth in the permafrost, or when σt, the product of conductivity and thickness, exceeds 0.02 mho. The effect of displacement currents depends on ϵ, which may be as high as $100\epsilon_0$ for ice below 10^4 hertz (ϵ_0 is the electrical permittivity of free space). For the general expression of the surface impedance of a two-layer and three-layer earth, see J. R. Wait, *Electromagnetic Waves in Stratified Media* (Pergamon, New York, 1962).
9. The average over N stations is

$$\bar{\rho}_N = \frac{1}{N^2}\left[\sum_{i=1}^{N}(\rho_i)^{1/2}\right]^2$$

10. D. F. Barnes and G. R. MacCarthy, *Preliminary Report on Tests of the Application of Geophysical Methods to Arctic Ground-Water Problems* (Open-file report, U.S. Geological Survey, Denver, Colo., 1964); A. A. Ogilvy, *Geol. Surv. Can. Econ. Geol. Rep. No. 26* (1970), pp. 641–648.
11. This work was primarily supported by the Canadian Defence Research Board while the author was under fellowship from the International Nickel Company; part of the equipment used was loaned by Kennecott Copper Corporation. Field support and logistics by W. J. Scott and the Geological Survey of Canada are gratefully acknowledged.

25 April 1975; revised 10 June 1975

Neutron Diffraction Analysis of Myoglobin: Structure of the Carbon Monoxide Derivative

Abstract. *The locations of hydrogen and deuterium atoms and water molecules have been investigated in carbon monoxide myoglobin using neutron diffraction, and the results are compared with earlier work on metmyoglobin. Parallel real space refinements on the two molecules show relatively few changes, but do show the carbon monoxide molecule with the iron atom moving into the heme plane.*

Studies of sperm whale metmyoglobin (metMb) (*1, 2*) show that the positions of hydrogen atoms, deuterium atoms, and bound water molecules in a protein can be determined by neutron diffraction. In contrast to x-ray scattering factors, the neutron scattering length of the hydrogen atom is negative, and large enough to be seen readily in a Fourier synthesis. In this report we describe a neutron diffraction analysis of carbon monoxide myoglobin (MbCO), a low-spin derivative.

According to Perutz (*3*), mammalian hemoglobin (Hb) undergoes significant structural changes on transition to the low-spin case. X-ray comparisons of Mb derivatives of high (*4*), intermediate (*5*), and low (*6, 7*) spin do not show such large changes, although *p*H-dependent differences occur in alkaline metMb (*8*). Hoard's prediction (*9*) that the low-spin ferrous iron is coplanar with the porphyrin [as observed for some porphyrin complexes (*10*)] has not been confirmed in any of these Mb studies. On the other hand, investigations of several Hb monomers (*11–13*) show structural changes with the iron in the heme plane. Neutron analysis allows examination of some of these questions, as well as the elucidation of the general hydrogen bonding, hydrogen-deuterium exchange, and the bound water structure.

Fig. 1. Section of the MbCO neutron Fourier maps, showing CD4 phenylalanine. The side chain is well formed and indications of hydrogen atoms appear as negative contours.

A large crystal of MbCO (27 mm^3) was grown from a 70 percent saturated ammonium sulfate solution at *p*H 5.7. The hydrogen atoms in the solvent (and thus in the water of hydration) were replaced with deuterium atoms after the crystal was grown, so as to reduce the background radiation resulting from the large incoherent neutron scattering of hydrogen. A neutron flux of 1.0×10^7 neutrons per square centimeter per second was obtained at 1.52 Å with a pyrolytic graphite monochromator. An identical crystal served as analyzer to reduce half-wavelength contamination and background. Counting statistics were improved compared to those in the metMb work by the higher reflectivity of pyrolytic graphite and longer exposure times. Over 14,000 reflections in the 1.8 Å half-sphere were measured by rotating the crystal in 0.06° steps with a four-circle diffractometer at the Brookhaven High Flux Beam Reactor. After background and Lorentz corrections, absorption corrections were applied using the experimentally determined value of the neutron absorption coefficient, $\mu = 2.4\ cm^{-1}$. The agreement factor for the 6706 independent reflections was 3.8 percent in the structure factor, *F*.

Neutron phases were calculated from the Kendrew-Watson x-ray structure (*14*) (no hydrogen atoms). These calculated phases should approximate the true neutron phases in spite of the fact that omitting the hydrogen atoms leaves out almost half the total number of atoms in the protein. This is due to the systematic distribution of hydrogen atoms throughout the protein. Phase calculations on a model Mb structure show the average phase error due to the omission of hydrogen and deuterium atoms to be only 31° to a Bragg resolution of 1.8 Å. Further verification comes from the anomalous determination of several hundred phases from a Cd metMb derivative (*15*), where an average phase change of 37° was observed when compared to the calculated phases described above. The calculated phases are therefore sufficiently accurate for an analysis of the H, D, and D_2O positions and for the initiation of a structure refinement.

Part of the MbCO Fourier map is depicted in Fig. 1, showing the CD4 phenylalanine side chain with evidence of hydrogen atoms that are bound to the aromatic ring. In general, the MbCO Fourier maps were clearer and less noisy than the metMb maps because of the larger data set and